Photoluminescence, optical absorption, and excitation spectra of cinnabar (α-HgS)

C. T. Simpson, W. Imaino, and W. M. Becker
Department of Physics, Purdue University, West Lafayette, Indiana 47907
(Received 7 February 1980)

In cinnabar (α-HgS) grown by chemical vapor transport (CVT), four photoluminescence (PL) features, X_1, X_2, B_1, and B_2, are observed with below band-gap photoexcitation. Two of these PL features, X_1 at 1.873 eV and X_2 at 1.855 eV, are sharp, with half-widths of 3.7 and 6.6 meV, respectively, and two of them, B_1 at 2.19 eV and B_2 at 1.78 eV, are broad, with half-widths of ~ 100 meV. New photoluminescence, optical absorption, and PL excitation measurements are reported on this material. The details observed in these measurements, together with transport results, enable presentation of an energy-level scheme and Fermi-level assignment for CVT-grown cinnabar which accounts for the X_1, X_2, B_1, and B_2 PL features. In addition to the valence- and conduction-band continua, five energy states are postulated, three levels nearer to the conduction band and two levels nearer to the valence band. The binding energies of the former are 0.005, 0.402, and 0.420 eV, and those of the latter are 0.25 and 0.05 eV. Based upon PL excitation spectra and optical absorption, ϵ_F, the equilibrium Fermi energy, is placed in the range $1.855 \lesssim \epsilon_F \lesssim 1.873$ eV. In order to explain the shape of the optical absorption and PL excitation spectra, matrix-element effects are examined for a very simple band-to-impurity absorption process. The two PL features X_1 and X_2 can be interpreted as bound-to-free transitions which are weakly coupled to lattice vibrations, whereas the B_1 and B_2 features can be interpreted as bound-to-bound transitions strongly coupled to lattice vibrations. The temperature dependence of the X_1 and B_2 peak intensities is discussed in terms of a configuration coordinate model. The linear broadening of the X_1 and X_2 peaks with temperature above ~ 20 K is attributed to interactions with phonons.

I. INTRODUCTION

Cinnabar, the trigonal form of mercury sulfide, is a wide-band-gap semiconductor whose crystal structure belongs to the space group $P3_121$ (D_3^4) (Ref. 1). Some of the interesting properties exhibited by cinnabar are a pronounced band edge dichroism,[2] a large birefringence,[3] remarkable optical activity,[4,5] and one of the strongest acousto-optic effects observed.[6] Because of the potential applications of cinnabar, it is important to establish the nature of native defects and/or chemical impurities introduced during the growth process.

Luminescence is a technique that has been shown to be a useful and often powerful tool to study electronic states in wide-band-gap semiconductors.[7,8] The luminescence of cinnabar has been studied by various groups employing electron-beam excitation[9-17] and above band-gap photoexcitation.[18] Using hydrothermally grown as well as naturally occurring cinnabar, these groups have investigated green, yellow, and red luminescence which they attribute variously to edge emission, impurity bands, and donor-acceptor pairs. For chemical vapor transport (CVT) grown mercury sulfide, excited by above band-gap radiation, we have reported[19] features similar to those seen by the above authors. In the same study, three new photoluminescence (PL) features were observed using below band-gap excitation, two sharp lines which we label X_1 and X_2 at $E(X_1) \simeq 1.873$ eV and $E(X_2) \simeq 1.855$ eV, and a broad band which we label B_2 at $E(B_2) \simeq 1.78$ eV. A second broad PL band which we label B_1 was observed at $E(B_1) \simeq 2.19$ eV for excitation energies in the range $1.87 \lesssim \hbar\omega_L \lesssim 1.96$ eV.

In this paper, we present a more complete series of experiments on synthetic CVT-grown cinnabar crystals than that reported earlier.[19] We emphasize optical measurements near $E(X_1)$, including both PL excitation spectroscopy and optical absorption. As a result of this work and the complementary transport measurements,[20] we are able to present an energy level scheme for certain states pertinent to the photoluminescence observed in CVT-grown cinnabar. Experimental details such as crystal preparation, impurity content, and spectroscopic techniques are presented in Sec. II. The experimental results of our measurements are given in Sec. III. In Sec. IV, we present the energy-level model and discuss each of the four PL features X_1, X_2, B_1, and B_2 in terms of this model, together with a discussion of the possible mechanisms for thermal quenching and broadening of the luminescence.

II. EXPERIMENTAL TECHNIQUES

The samples studied in this investigation were grown by Faile[21] using a closed-tube chemical-vapor-transport technique. During a run the growth region of the closed tube was always maintained below the structural phase transition temperature of cinnabar (618 ± 2 K) (Ref. 22). Growth

runs of two weeks employing iodine and NH_4Cl as transport agents yielded a sufficient quantity of crystals for our study. Both dendritic and tabular habit (TH) crystals usually occur in a single growth run. Since the PL features excited by below band-gap excitation were observed only in the TH crystals, we emphasize our results on these samples. In contrast to the dendrites, the TH crystals are generally of good optical quality except for a line of voids or liquidlike inclusions lying along the $[10\bar{1}0]$ growth direction.[23] Tabular habit sample volumes ranged up to ~5 mm^3 with a typical sample having dimensions $0.3\times1\times2$ mm^3. The largest crystal face was bounded by the basal plane $c\{0001\}$. Other prominent forms present in the TH samples were $r\{10\bar{1}1\}$, $-r\{01\bar{1}1\}$, and $m\{10\bar{1}0\}$ (Ref. 24). For our PL measurements, the sample surfaces were as-grown. The propagation direction of the exciting radiation and observed luminescence was parallel to the c axis; similarly, the optical absorption was measured with light propagating parallel to the c axis.

Several reports on synthetic crystals of cinnabar have appeared in the literature; however, attempts to correlate deliberately added chemical dopants with specific energy states are inconclusive.[14,15] In our previous work,[19] we attempted to identify specific impurities responsible for the new PL features observed in synthetic TH cinnabar crystals. Iodine was found to be the dominant impurity in these CVT-grown samples; however, further impurity analysis has shown that the presence of iodine does not guarantee the existence of the X_1, X_2, B_2 PL features. For example, the iodine concentration of TH and dendritic crystals is approximately the same (~10^{19} cm^{-3}), whereas only the TH crystals exhibit the X_1, X_2, B_2 PL emission.

Spark source mass spectrographic analyses were performed on a number of samples in order to determine if specific impurities might be associated with the observed PL spectrum. Results given in Table I exhibit the impurity concentration in polycrystalline HgS synthesized from Hg (99.9999999% purity) and S (99.9999% purity), and typical TH crystals. Two comments may be made concerning this impurity analysis: First, the CVT-grown crystals clearly show the overwhelming presence of the iodine transport agent; second, even though chlorine, introduced as NH_4Cl, was also employed as a transport agent for CVT growth, the concentration of Cl is roughly the same in both synthesized HgS and the CVT-grown material. Further work on the crystal-growth technology is needed before any definite correlation can be made between PL spectra and impurity content.

The techniques used to measure the photoluminescence and excitation spectra are basically the same as those used in our earlier resonant Raman study of cinnabar.[25] For the optical absorption measurement, broad-band radiation from a tungsten lamp was passed through the sample. The spectral transmission of the sample was measured with a double spectrometer system described previously.[25] Using the identical geometry, the broad-band radiation was passed through the system without the sample. Using these two spectra and the known refractive index dispersion,[3] we calculated the absorption coefficient. Because the absorption of the sample was weak, we multiscanned the spectral region of interest and employed a multichannel analyzer[25] in order to achieve an adequate signal-to-noise ratio.

For the PL measurements, the samples were either immersed in superfluid liquid helium or mounted on the cold finger of a three-window optical glass cryostat.[26] The cold finger was in contact with the cryogenic bath, either liquid He or liquid N_2. Attached to the cold finger but thermally isolated from it via a sheet of teflon was a copper block onto which the sample was mounted. The temperature of this block and consequently that of the sample could be raised above that of the bath by means of a manganin heater. A light-emitting-diode sensor[27] inserted into the copper block was used to measure the sample temperature.

TABLE I. Impurity concentration ($\times10^{18}cm^{-3}$) by spark source mass spectrographic analysis of (a) HgS synthesized from Hg (99.9999999% purity) and S (99.9999% purity) and (b) tabular habit crystals (analysis performed by Battelle Memorial Institute).

Element	Sample (a)	Sample (b)
Li	0.14	0.0014
B	0.0045	0.0090
Na	6.4	1.1
Mg	0.10	0.040
Al	≤0.090	≤0.090
Si	0.052	0.052
P	0.047	0.016
Cl	6.9	1.4
K	0.062	0.062
Ca	0.12	0.12
Ti	0.10	0.010
Cr	0.0094	≤0.00094
Mn	0.0089	0.0046
Fe	0.18	0.18
Cu	1.5	0.0077
Zn	<0.15	<0.15
As	0.0065	<0.0013
I	0.0019	38.4

III. EXPERIMENTAL RESULTS

An example of the spectra produced by below band-gap excitation is shown in Fig. 1. This fig-

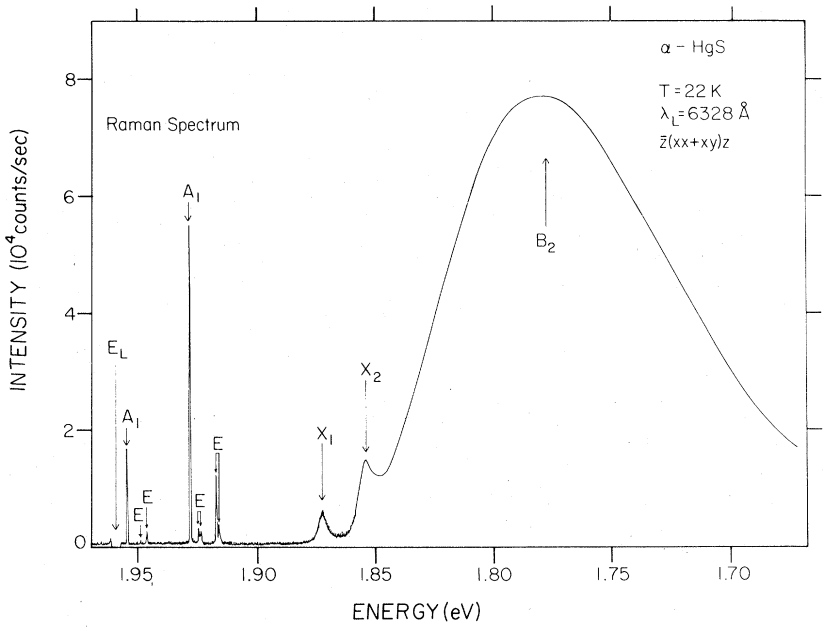

FIG. 1. Photoluminescence and Raman-scattering spectrum of cinnabar excited by $\hbar\omega_L = 1.959$ eV ($\lambda_L = 6328$ Å) radiation at 22 K. See Refs. 25 and 28 for details of the Raman spectrum.

ure exhibits both the Raman and the PL spectra of cinnabar at $T = 22$ K for exciting radiation $\hbar\omega_L$ equal to 1.959 eV ($\lambda_L = 6328$ Å). The Raman spectrum has been discussed elsewhere[25,28] and is shown here only for comparison. We focus our attention on the behavior of the X_1-X_2-B_2 PL structure. This structure was observed in a variety of TH crystals from different growth runs; in contrast, it was not observed either in dendritic crystals from the same growth runs as the TH crystals, or in natural cinnabar specimens. At 22 K, the peak energies of the X_1, X_2, and B_2 features are $E(X_1) = 1.872$ eV, $E(X_2) = 1.854$ eV, and $E(B_2) = 1.78$ eV, with half-widths (full width at half-maximum, FWHM) of 3.7, 6.6, and 113 meV, respectively. In certain TH samples at $T \sim 2$ K, the X_2 peak was weaker in intensity than the X_1 peak. For such samples, we observed several weak PL structures, approximately one-twentieth the intensity of X_1 between $E(X_1)$ and $E(X_2)$. From their energy positions, we identify these structures as weak phonon sidebands of the X_1 emission. Similar weak sidebands of the X_2 emission could not be observed presumably because of the strong B_2 emission.

As we reported previously,[19] the shift of the X_1 and X_2 peak energies with temperature, approximately -0.3 meV/K, is about one-half the closure rate of the band gap. In our previous work, we reported that the widths of X_1 and X_2 increase linearly with temperature in the range $20 \lesssim T \lesssim 80$ K.

Figure 2 shows explicitly the FWHM of X_1 and X_2 as a function of temperature. In the linear region, the FWHM of X_1 increases at the rate of 0.25 meV/K and that of X_2 increases at the rate of 0.46 meV/

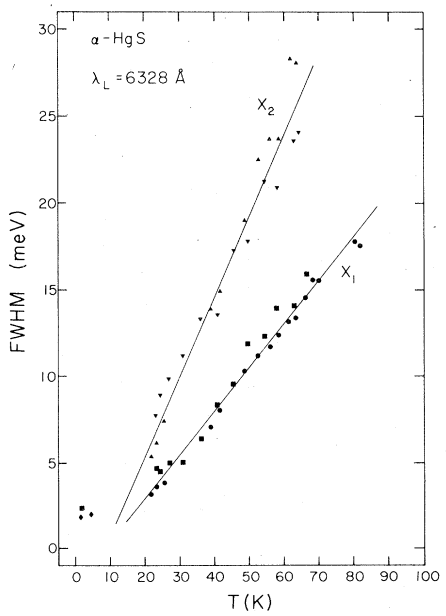

FIG. 2. Full width at half-maximum (FWHM) of the X_1 and X_2 photoluminescence structures as a function of temperature for exciting radiation $\hbar\omega_L = 1.959$ eV ($\lambda_L = 6328$ Å). The straight lines are least-squares fits to the data for $T \gtrsim 20$ K.

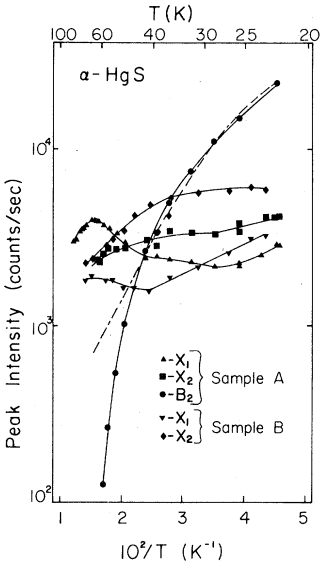

FIG. 3. Peak intensities of the X_1, X_2, and B_2 photoluminescence in sample A and the X_1 and X_2 photoluminescence in sample B as a function of temperature. The dashed curve is a plot of Eq. (5) using the parameters given in the text. The solid lines are drawn for clarity.

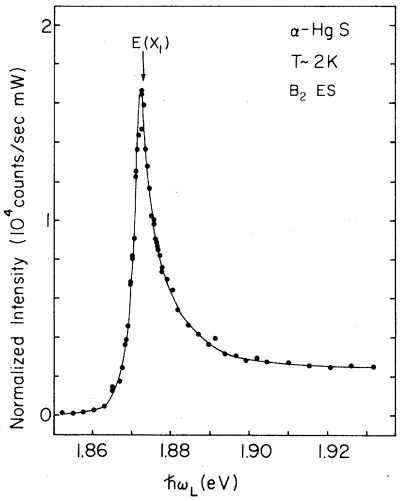

FIG. 4. Excitation spectrum (ES) of the B_2 photoluminescence peak as a function of exciting dye laser energy $\hbar\omega_L$ in the vicinity of $E(X_1)$, the X_1 emission energy. The solid line is drawn for clarity.

K. The FWHM of both X_1 and X_2 extrapolate to zero at about 8.1 K. In addition to the linear region above 20 K, we show the FWHM of the X_1 peak at low temperatures. These data suggest that, at least for X_1, the FWHM becomes temperature independent at low temperatures. Furthermore, these as well as other results show that the FWHM is larger than a few meV even at superfluid helium temperatures.

The peak intensities of the X_1, X_2, and B_2 PL features are plotted as a function of reciprocal temperature in Fig. 3. Sample A and sample B represent two TH samples from the same growth run. The intensity of the B_2 band, shown in the figure for sample A, drops by over two orders of magnitude on going from 20 to 60 K. On the other hand, the X_1 and X_2 peak intensities do not appreciably decrease until the temperature exceeds ~80 K. We do not observe thermalization between X_1 and X_2 at temperatures below 20 K. Activation energies which can be associated with the B_2 peak intensity are ~6–7 meV at the lowest temperatures and ~80 meV at the highest temperatures. The X_1 peak intensity in both samples exhibits a maximum near 67 K. From the behavior of sample A, it is clear that this increase in the X_1 intensity occurs in a temperature region where the B_2 band is strongly decreasing.

We exhibit in Fig. 4 the excitation spectrum of the B_1 PL band for dye laser energies in the range 1.85 to 1.93 eV. This spectrum shows that the B_2 PL band is strongly correlated with optical transitions into states that are also associated with the X_1 luminescence. The absence of structure at $E(X_2)$ indicates there is no excitation via optical transitions into states associated with the X_2 luminescence. Furthermore, the absence of structure in the region $\hbar\omega_L > E(X_1)$ indicates that excitation via phonons into states associated with the X_1 PL is weak. From the persistence of the B_2 intensity for dye laser energies $\hbar\omega_L$, well above $E(X_1)$, we conclude that a continuum of states is involved in the excitation process.

In Fig. 5, we show the excitation spectra of X_1, X_2, B_1, and B_2. As in the case of the B_2 excitation spectrum, the X_2 and B_1 excitation spectra are correlated with states associated with the X_1 luminescence. Characteristics common to the X_2, B_1, and B_2 PL features include a dramatic increase in PL intensity as $\hbar\omega_L$ approaches $E(X_1)$ from the low energy side, a peak in PL intensity for $\hbar\omega_L = E(X_1)$, and a gradual decrease in PL intensity for $\hbar\omega_L > E(X_1)$. We conclude from the similarity of the excitation spectrum of all three PL features that the same excitation mechanism is involved in all three luminescence processes. The limited data shown for the X_1 PL has the same form as the excitation spectra for the other three PL features.

In an attempt to understand the nature of the B_2 emission, we have studied the peak energy of the band as a function of $\hbar\omega_L$. The result of this mea-

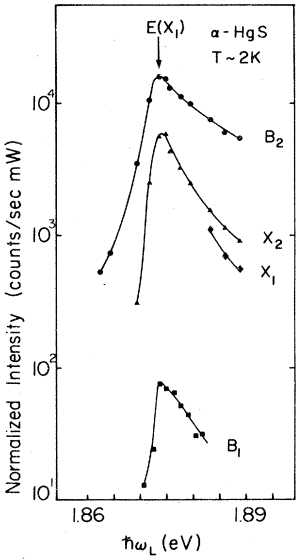

FIG. 5. Excitation spectra of the X_1, X_2, B_1 and B_2 photoluminescence peaks as a function of exciting dye laser energy $\hbar\omega_L$. The solid lines are drawn for clarity.

surement is plotted in Fig. 6. For $\hbar\omega_L > 1.89$ eV, the peak energy $E(B_2)$ is roughly constant. As $\hbar\omega_L$ approaches $E(X_1)$, $E(B_2)$ increases; $E(B_2)$ at $\hbar\omega_L \sim E(X_1)$ is about 13 meV larger than the $E(B_2)$ for $\hbar\omega_L \sim 1.89$ eV. From Fig. 4, the intensity of the B_2 PL is a maximum at $\hbar\omega_L \sim E(X_1)$. Thus for roughly constant dye laser intensity, the B_2 PL is excited more strongly for $\hbar\omega_L \sim E(X_1)$ than for $\hbar\omega_L > E(X_1)$.

The optical absorption in the vicinity of the X_1 PL feature is shown in Fig. 7. For comparison, we present the X_1 PL in this same energy range. Clearly, both the PL and optical absorption exhibit a peak at $E(X_1)$. The absorption peak, reminiscent of the excitation spectra, appears asymmetric toward higher energies. Optical absorption measurements over the range 1.85 to 1.90 eV failed to reveal any additional structure.

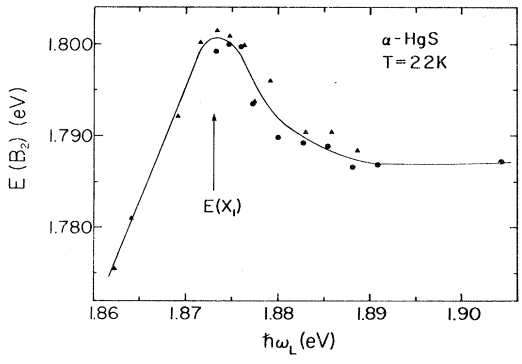

FIG. 6. Peak position of $E(B_2)$ as a function of dye laser energy $\hbar\omega_L$ at 22 K. The solid line is drawn for clarity.

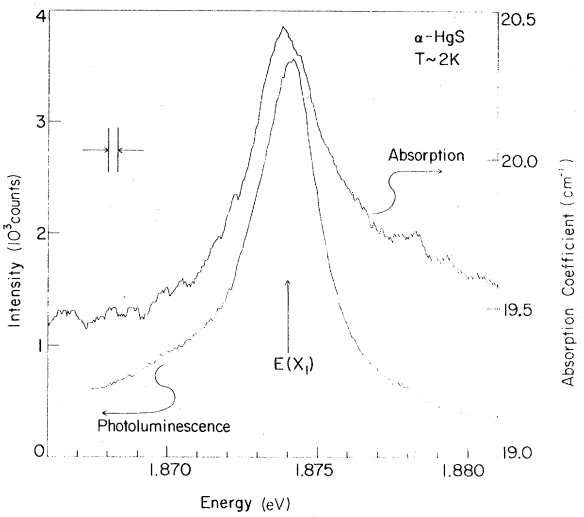

FIG. 7. Optical absorption (top curve) and photoluminescence (bottom curve) at 2 K in the vicinity of the X_1 photoluminescence peak.

IV. DISCUSSION

Seebeck coefficient measurements on our CVT-grown cinnabar indicate that the samples are *n* type. The temperature dependence of the Seebeck coefficient and the resistance in the range 300–500 K yields an equilibrium Fermi energy on the order of one-half eV from the conduction band edge.[20]

The coincidence of the peak at $E(X_1)$ for both absorption and emission, as exhibited in Fig. 7, indicates that the transition responsible for these features is electronic in nature. From the asymmetry towards higher energy of both the absorption and excitation spectra, we conclude that the transition is between a discrete state and a continuum. The absence of absorption at $E(X_2)$, the existence of PL emission at $E(X_2)$, and the peak in the X_2 excitation spectrum at $E(X_1)$ suggests that the initial discrete state involved in the X_2 emission is near the discrete state responsible for the X_1 emission. From these considerations, we postulate two discrete donor states, labeled 2 and 3 in Fig. 8. Again, since there exists absorption into level 2 but not into level 3, we position ϵ_F, the equilibrium Fermi level, between these two states.

As shown in Fig. 3, the peak intensity of the B_2 band has a temperature dependence distinctly different from that of X_1 and X_2. We believe this difference, as well as the much greater half-width

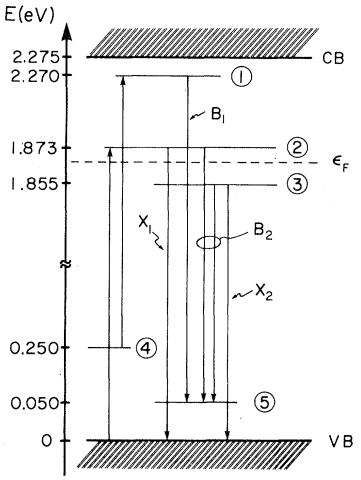

FIG. 8. Energy-level scheme for tabular habit CVT-grown cinnabar crystals. Energy states labeled 1—5 lie within the forbidden energy gap. The valence-band (VB) and conduction-band (CB) continua are represented by cross-hatching. The position of the equilibrium Fermi energy ϵ_F is indicated by a dashed line. Approximate energy values (not drawn to scale) are shown on the left side of the figure.

of B_2, implies that the recombination process responsible for B_2 is different from that for X_1 and X_2. Instead of a donor-to-valence band transition, as in the case of the X_1 and X_2 recombination, B_2 arises from a donor-acceptor transition. We place an acceptor state which we label 5 in Fig. 8, at approximately 0.050 eV above the valence band.

We postulate level 1 in order to account for the B_1 up-converted band.[29] Level 4 is included in our scheme to account for the 1.9-eV PL band observed in our TH CVT-grown samples using above band-gap photoexcitation.[19] States similar in energy to level 1 and level 5 have been used to describe the behavior of a yellow emission band in natural cinnabar.[17] Also, a state similar in energy to level 4 has been associated with a 1.9-eV emission band in natural cinnabar specimens excited by an electron beam[12] or by above band-gap light.[18]

The excitation and recombination processes responsible for the X_1, X_2, B_1, and B_2 PL features can now be examined in terms of the energy states 1–5 presented in Fig. 8. The electronic transition responsible for the excitation of the X_1, X_2, and B_2 luminescence is that of an electron from the valence band into level 2. This excitation process clearly has the characteristics we observe in the X_1, X_2, B_2 PL excitation spectra: Namely, there is no excitation for $\hbar\omega_L < E_2$, where $E_2 = E(X_1)$ is the energy of state 2 above the valence band, there is a peak in the excitation for $\hbar\omega_L \sim E_2$ due to a matrix element effect, and the excitation persists for $\hbar\omega_L > E_2$ because the initial state for the electron is the valence-band continuum. Transitions into level 3 are not possible because ϵ_F is above level 3; that is, in equilibrium at low temperature, level 3 is already occupied. We believe that the energy-level scheme described here also applies to the CVT-grown dendritic crystals. In such samples, however, the absence of the X_1, X_2, and B_2 PL is a consequence of ϵ_F being above level 2. This results from weaker compensation in the dendrites as compared to the TH crystals.

The excitation of the B_1 up-converted band[29] can be understood, within the framework of the energy-level scheme presented here, in terms of a two-step excitation process. First, an electron is excited from level 4 to level 1; more or less simultaneously, an electron is excited from the valence band into level 2. The free hole is captured by level 5 with the B_1 emission resulting from the recombination of the electron in level 1 with the hole in level 5. Because the excitation requires two steps, the resulting emission should be weak; indeed, as we have shown previously[19] the B_1 emission intensity is ~50 times weaker than the B_2 emission intensity. Also, the B_1 excitation spectrum shown in Fig. 5 is similar to that of X_1, X_2, and B_2 because, like these latter PL features, the valence-band to level 2 electronic transition is an essential step in the excitation process.

The excitation of an electron into level 2 leaves a hole in the valence band. This free hole can recombine in two possible ways: It can recombine either with the electron excited into level 2 or with the electron occupying level 3. The first process yields the X_1 emission and the second yields the X_2 emission.

Free hole capture by level 5 is an essential step leading to the B_2 recombination. This hole can then recombine with either the electron in state 2 or the electron in state 3. Both of these luminescence channels are donor-acceptor recombination processes.[30,31] Due to the Coulomb attraction between the ionized donor and ionized acceptor the binding energy of an electron-hole pair is reduced by $e^2/\epsilon R$, where e is the electronic charge, ϵ is the static dielectric constant, and R is the donor-acceptor pair separation. The emitted radiation $\hbar\omega_{ij}$ for the ith donor and jth acceptor is given in the simplest form as

$$\hbar\omega_{ij} = E_g - (E_d + E_a) + e^2/\epsilon R_{ij} . \quad (1)$$

For large R_{ij}, and neglecting interactions with lattice vibrations, the discrete $\hbar\omega_{ij}$ merge into a broad band; for example, in GaP (Ref. 30) such a band has a width of ~20–30 meV. Consider now the interaction of this zero-phonon band with lat-

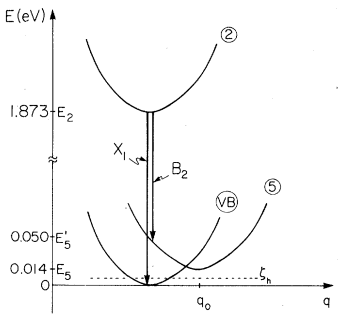

FIG. 9. Configuration coordinate diagram for the valence band (VB), level 5 and level 2. The quasi-Fermi level for holes ζ_h is indicated by a dashed line. The X_1 and B_2 recombination processes are represented by downward arrows. Approximate energy values (not drawn to scale) are shown on the left edge of the figure.

tice vibrations. In the simplest model the intensity of the nth phonon sideband can be written[32]

$$I_n = S^n e^{-S}/n! , \tag{2}$$

where S is the electron-phonon coupling parameter. Weak coupling is characterized by $S<1$ thus exhibiting dominant zero-phonon emission, and strong coupling is characterized by $S\gg1$ with the dominant emission being ~S phonon energies less than the zero-phonon energy. In the case of GaP, the coupling is weak and there is only one LO phonon. This results in the observation of only one phonon sideband series.[30] In cinnabar there are eight LO phonons and thus eight possible series of phonon sidebands.[33] The mechanism we propose for the broad B_2 band is a donor-acceptor transition with strong electron-phonon coupling. The zero-phonon transitions are between level 2 and level 5, or level 3 and level 5, or both. We cannot distinguish between the two processes because of the lack of structure in the B_2 emission.

The temperature dependence of the B_2 PL intensity shown in Fig. 3 can be understood in terms of a configuration coordinate model with two competing recombination processes, namely, X_1 and B_2. In Fig. 9 we exhibit the configuration coordinate diagram for this model. Considering only these two recombination processes, we write the B_2 recombination efficiency $\eta(B_2)$ as[34]

$$\eta(B_2) = \frac{P_{25}N_2 f_2 N_5(1-f_5)}{P_{25}N_2 f_2 N_5(1-f_5)+P_{20}N_2 f_2 N_0(1-f_0)} , \tag{3}$$

where P_{ij} is the transition probability of the i to j transition, N_k is the density of kth states, f_i is the occupation probability of the ith initial state for electrons, $(1-f_j)$ is the occupation probability of the jth final state for holes, and the subscript zero refers to valence band states. Here the f_i's are for steady-state nonequilibrium conditions characterized by ζ_e, the quasi-Fermi level for electrons, and ζ_h, the quasi-Fermi level for holes. At sufficiently low temperatures this expression can be written

$$\eta(B_2) \simeq \frac{1}{1+(P_{20}N_0/P_{25}N_5)\exp(-E_5/kT)} . \tag{4}$$

Using this expression and assuming the P_{ij} and N_k are temperature independent, we write the B_2 PL intensity

$$I(T) \simeq \frac{I_0}{1+\rho\exp(-E_5/kT)} . \tag{5}$$

A nonlinear least-squares fit of our experimental B_2 intensity data to Eq. (5) yielded the following parameters:

$$I_0 = 3.3 \pm 0.4 \times 10^4 ,$$

$$\rho = 5.5 \pm 2.0 \times 10^2 ,$$

$$E_5 = 13.8 \pm 1.3 ,$$

where I_0 is measured in counts/sec and E_5 in meV. The dashed curve in Fig. 3 is a plot of Eq. (5) using the parameters given above. Good agreement between the model and experimental data exists at low temperatures. The lack of agreement at higher temperatures may be related to processes not taken into account by this model.

The energy E_5 (≃14 meV) obtained from the above analysis is considerably smaller than the energy E_5' (≃50 meV) taken from the energy position of the B_2 luminescence. The reason for this discrepancy is clearly explained by Fig. 9; E_5 (≃14 meV) is the thermal ionization energy of a hole from the minimum of the level 5 potential energy curve to the valence band, whereas E_5' (≃50 meV) is the energy on the level 5 potential energy curve to which optical transitions having $\Delta q \sim 0$ are made. The physical mechanism responsible for the decrease in B_2 PL intensity and concurrent increase in X_1 PL intensity is the thermal redistribution of holes from level 5 into the valence band with increasing temperature.

As shown by Thomas *et al.*,[30] the peak energy of a broad donor-acceptor band shifts to higher energy as the excitation intensity is increased. This shift is ascribed to the saturation of the distant pair recombination. The result shown in Fig. 6 further supports the donor-acceptor model for the B_2 PL band. From Fig. 4 we see that the B_2 band is excited more strongly for $\hbar\omega_L \sim E(X_1)$ than for $\hbar\omega_L > E(X_1)$. Because of this stronger pumping at $\hbar\omega_L \sim E(X_1)$, the peak energy of B_2 shifts to higher energy. For fixed $\hbar\omega_L$ greater than $E(X_1)$, pre-

liminary measurements suggest that $E(B_2)$ shifts to higher energy as the excitation intensity is increased, a fact consistent with the above interpretation.

In order to account for the peak in the optical absorption and the excitation spectrum at $\hbar\omega_L \sim E(X_1)$, we have performed a simple model calculation of band-to-impurity absorption in cinnabar. Following general considerations of optical absorption as outlined by Johnson[35] and Bebb and Williams,[36] we treat band-to-impurity absorption using the approach of Eagles[37] and Dumke.[38] Within this framework, we can write the absorption coefficient arising from band-to-impurity transitions as

$$\alpha(\hbar\omega) \simeq \frac{C}{E_g - E_d + a(1-\gamma k)k^2} \frac{a_0^3}{(1+a_0^2k^2)^4} \frac{k}{a(1-\frac{3}{2}\gamma k)}, \tag{6}$$

where C represents all constants and weakly varying quantities, $E_g - E_d + a(1-\gamma k)k^2$ represents the $1/\hbar\omega$ dependence of $\alpha(\hbar\omega)$, a_0 is an effective radius of the impurity wave function, and $k/a(1-\frac{3}{2}\gamma k)$ represents the valence-band density of states. We use a valence-band energy dispersion relation $E_v = -a(1-\gamma k)k^2$, where the numerical values of a and γ are taken from the energy-band dispersion curves of cinnabar given by Doni *et al.*[39] Because the electron occupation factor $f_i f_f' - f_f f_i' = f_i - f_f$ is a weak function of $\hbar\omega$ on the order of one, we include it in the constant C.

Having little detailed knowledge of the impurity center, we have stressed simplicity in our calculation. We have neglected any spread in the impurity density of states and we write the impurity wave function as a simple product of an exponential $1s$-like envelope function with a single conduction-band Bloch function. The matrix elements calculated using these simple wave functions yield the second factor in Eq. (6).

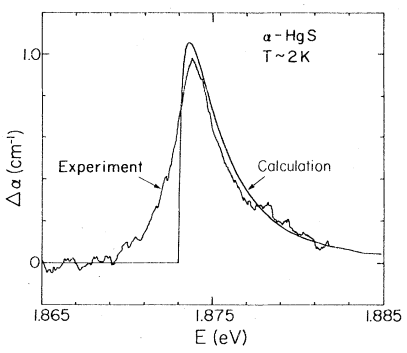

FIG. 10. Comparison of the experimental optical absorption in the vicinity of $E(X_1)$ with a model calculation using Eq. (6) for parameters given in the text.

In Fig. 10, we exhibit the experimental absorption structure, $\Delta\alpha$ (with the flat background subtracted), and the model calculation for $\alpha(\hbar\omega)$. We used a nonlinear least-squares fitting procedure to calculate the parameters C and a_0 from our experimental data. The values we obtained for these parameters are

$$C = 3.61\times10^{-2}\ \text{eV}^2\,\text{cm}^{-1},$$

$$a_0 = 1.10\times10^{-7}\ \text{cm} = 11.0\ \text{Å}.$$

Within a hydrogenic effective-mass theory, we can estimate the conduction-band effective mass using the expression

$$\frac{m^*}{m} \simeq \bar{\kappa}\left(\frac{a_B}{a_0}\right), \tag{7}$$

where a_B (=0.53 Å) is the atomic hydrogen Bohr radius and $\bar{\kappa}$ (=17.8) is the static dielectric constant.[40] Using the above value of a_0 we obtain $m^*/m \simeq 0.9$ which is in good agreement with the conduction-band effective mass obtained from the energy-band dispersion curves of Doni *et al.*[39] ($m^*/m \simeq 0.8$). We have considered the Sommerfeld enhancement factor of the form[41] $(2\pi/\varkappa a_0)[1-\exp(-2\pi/\varkappa a_0)]^{-1}$, where $\varkappa$ characterizes one of the electron states in the conduction band. The effective radius of the impurity wave function we get using this enhancement factor, $a_0 = 11.6$ Å, is very nearly the same as that obtained without the enhancement factor; for this reason, we do not include it in Eq. (6).

We consider the thermal broadening of the X_1 and X_2 PL, as shown in Fig. 2, to be a lifetime effect, that is, due to the electron-phonon interaction the excited-state lifetime is reduced, yielding a broadened line shape.[42] The temperature dependence of the width $h(T)$ can be written as[42,43]

$$h(T) = \frac{h_0}{1-\exp(-T_c/T)}, \tag{8}$$

where h_0 is the low-temperature width and T_c is a critical temperature below which the width becomes approximately constant. In the high-temperature limit, $T \gg T_c$, we find

$$h(T) \simeq (h_0/T_c)\,T, \tag{9}$$

and in the low-temperature limit, $T \ll T_c$, we get

$$h(T) \simeq h_0. \tag{10}$$

From the linear region of our data, as shown in Fig 2, we find for X_1 $h_0/T_c \simeq 0.25$ meV/K, and from the width at low temperature, we find $h_0 \simeq 2$ meV; for X_2, we get $h_0/T_c \simeq 0.46$ meV/K. Using these values for X_1, we calculate $T_c \simeq 8$ K. Also, from the relative widths of the X_1 and X_2 emission, we conclude that the lifetime of the electron in level 3 is less than that of an electron in level 2.

V. CONCLUSION

We have presented new experimental measurements on synthetic CVT-grown cinnabar. These include photoluminescence, excitation spectroscopy, and optical absorption near moderately deep electronic states within the forbidden gap. Based upon our experimental results, we have formulated an energy-level scheme capable of describing the behavior of these electronic states; in particular, this model explains (a) the temperature dependence of B_2 PL intensity, (b) the sharp rise in PL excitation of all four luminescence features, X_1, X_2, B_1, and B_2 at $E(X_1)$, (c) the persistence of the PL excitation to energies considerably above $E(X_1)$, and (d) the shape of the optical absorption and photoluminescence near $E(X_1)$.

ACKNOWLEDGMENTS

We are indebted to Dr. S. P. Faile for supplying the crystals used in this investigation. Appreciation is expressed to Dr. L. Resca and Professor S. Rodriguez for useful discussions. We thank Professor A. K. Ramdas for a critical reading of the manuscript. This work was supported by the NSF-MRL Program No. DMR 77-23798 and the National Science Foundation Grant No. DMR 77-27248.

[1]K. L. Aurivillius, Acta Chem. Scand. 4, 1413 (1950). $P3_121$ (D_3^4) is the space group for the right-handed form; the enantiomorphic left-handed form belongs to the space group $P3_221$ (D_3^6).

[2]R. Zallen, in *II-VI Semiconducting Compounds*, edited by D. G. Thomas (Benjamin, New York, 1967), p. 877.

[3]W. L. Bond, G. D. Boyd, and H. L. Carter, Jr., J. Appl. Phys. 38, 4090 (1967).

[4]B. Ayrault, F. Lefin, H. Langlois, Y. Toudic, and J. F. Palmier, Opt. Commun. 5, 239 (1972).

[5]H. Langlois, B. Ayrault, F. Lefin, and Y. Toudic, Phys. Status Solidi B 60, 821 (1973).

[6]J. Sapriel, Appl. Phys. Lett. 19, 533 (1971).

[7]P. J. Dean, J. Phys. (Paris) 35, 127 (1974).

[8]R. A. Street and W. Senske, Phys. Rev. Lett. 37, 1292 (1976).

[9]J. P. Noblanc, J. Loudette, and G. Duraffourg, Solid State Commun. 5, 803 (1967).

[10]G. Masse, J. P. Aicardi, J. P. Leyris, C. Butte, and F. Bombre, C. R. Acad. Sci. Ser. B 278, 85 (1974).

[11]G. Masse, J. P. Aicardi, and F. Bombre, C. R. Acad. Sci. Ser. B 279, 669 (1975).

[12]J. P. Aicardi, G. Masse, and M. Egee, Phys. Status Solidi A 32, 701 (1975).

[13]J. P. Aicardi, J. P. Leyris, G. Masse, and C. Butte, C. R. Acad. Sci. Ser. B 284, 57 (1977).

[14]J. P. Aicardi, J. P. Leyris, and G. Masse, Phys. Status Solidi A 39, 125 (1977).

[15]G. Masse, J. P. Aicardi, and J. P. Leyris, Phys. Status Solidi A 43, 191 (1977).

[16]J. P. Aicardi, J. P. Leyris, and G. Masse, J. Lumin. 16, 201 (1978).

[17]G. Masse, J. P. Aicardi, and J. P. Leyris, J. Lumin. 17, 29 (1978).

[18]G. G. Roberts and R. Zallen, J. Phys. C 4, 1890 (1971).

[19]C. T. Simpson, W. I. Imaino, W. M. Becker, and S. P. Faile, Solid State Commun. 28, 39 (1978).

[20]G. M. Joshi, Ph.D. thesis, Purdue University, 1980 (unpublished).

[21]S. P. Faile, J. Cryst. Growth 43, 129 (1978). See also M. M. Kreitman, S. P. Faile, C. W. Litton, and D. C. Reynolds, in *Proceedings of the International Conference on the Optical Properties of Highly Transparent Solids*, edited by S. S. Mitra and B. Bendow (Plenum, New York, 1975), p. 179.

[22]G. Kullerud, Carnegie Inst. Wash. Yearb. 64, 193 (1965); F. W. Dickson and G. Tunell, Am. Mineral. 44, 471 (1959).

[23]R. Aragon (private communication).

[24]We thank G. Hamill and G. Donnay for identifying the crystal forms.

[25]W. Imaino, C. T. Simpson, W. M. Becker, and A. K. Ramdas, Phys. Rev. B 21, 634 (1980).

[26]P. Fisher, W. H. Haak, E. J. Johnson, and A. K. Ramdas, in *Proceedings of the Eighth Symposium on the Art of Glassblowing* (American Scientific Glass Blowers Soc., Wilmington, Del., 1963), p. 136. The immersion cryostat used in this work is a modified version designed by R. J. Briggs.

[27]B. F. Griffing and S. A. Shivashankar, Rev. Sci. Instrum. 48, 1225 (1977).

[28]R. Zallen, G. Lucovsky, W. Taylor, A. Pinczuk, and E. Burstein, Phys. Rev. B 1, 4058 (1970); M. A. Nusimovici and A. Meskaoui, Phys. Status Solidi B 58, 121 (1973); M. A. Nusimovici and G. Gorre, Phys. Rev. B 8, 1648 (1973); Y. Marqueton, B. Ayrault, E. A. Decamps, and Y. Toudic, Phys. Status Solidi B 60, 809 (1973).

[29]We refer to Fig. 1 of Ref. 19 for a picture of the B_1 PL band.

[30]D. G. Thomas, M. Gershenzon, and F. A. Trumbore, Phys. Rev. 133, A269 (1964).

[31]F. E. Williams, J. Phys. Chem. Solids 12, 265 (1960).

[32]J. J. Hopfield, J. Phys. Chem. Solids 10, 110 (1959).

[33]Cinnabar has three A_2 (LO) phonons at 4.8, 17.5, and 44.3 meV and five E(LO) phonons at 6.0, 11.3, 18.2, 35.7, and 43.4 meV. See Ref. 28 for further details.

[34]J. I. Pankove, *Optical Processes in Semiconductors* (Dover, New York, 1975), p. 166.

[35]E. J. Johnson, in *Semiconductors and Semimetals*, edited by R. K. Willardson and A. C. Beer (Academic, New York, 1967), Vol. 3, p. 153.

[36]H. B. Bebb and E. W. Williams, in *Semiconductors and Semimetals*, edited by R. K. Willardson and A. C. Beer (Academic, New York, 1972), Vol. 8, p. 181.

[37]D. M. Eagles, J. Phys. Chem. Solids 16, 76 (1960).

[38]W.P. Dumke, Phys. Rev. 132, 1998 (1963).

[39]E. Doni, L. Resca, S. Rodriguez, and W. M. Becker, Phys. Rev. B 20, 1663 (1979). We thank L. Resca for providing numerical details of this calculation.

[40]We use $\bar{\kappa} = \frac{1}{3}(\epsilon_s^{\parallel} + 2\epsilon_s^{\perp})$ where the values of $\epsilon_s^{\parallel}$ and $\epsilon_s^{\perp}$ were calculated from the high-temperature values

given by Y. Marqueton, B. Ayrault, E. A. Decamps, and Y. Toudic, Phys. Status Solidi B 60, 809 (1973).
[41]G. Ascarelli and S. Rodriguez, Phys. Rev. 124, 1321 (1961). The enhancement factor we used comes from the corrected form of Eq. (A5) given by these authors.
[42]K. Colbow, Can. J. Phys. 41, 1801 (1963).
[43]R. Barrie and K. Nishikawa, Can. J. Phys. 41, 1823 (1963).